

Examples of renormalization group transformations for image sets

Samuel Foreman*

*Department of Physics and Astronomy, The University of Iowa, Iowa City IA 52242 and
Computational Sciences Division, Argonne National Laboratory, Argonne, IL 60439 USA*

Joel Giedt†

*Department of Physics, Applied Physics and Astronomy,
Rensselaer Polytechnic Institute, 110 8th Street, Troy NY 12180 USA*

Yannick Meurice‡

Department of Physics and Astronomy, 514 Van Allen Hall, The University of Iowa, Iowa City IA 52242

Judah Unmuth-Yockey§

Department of Physics, Syracuse University, Syracuse, NY 13244 USA

(Dated: October 26, 2018)

Using the example of configurations generated with the worm algorithm for the two-dimensional Ising model, we propose renormalization group (RG) transformations, inspired by the tensor RG, that can be applied to sets of images. We relate criticality to the logarithmic divergence of the largest principal component. We discuss the changes in link occupation under the RG transformation, suggest ways to obtain data collapse, and compare with the two state tensor RG approximation near the fixed point.

Keywords: Machine learning, Ising model, principal component analysis, worm algorithm, renormalization group

I. INTRODUCTION

Machine learning (ML) is a general framework for recognizing patterns in data without detailed human elaboration of the rules for doing so. As an example, a very general function, with many parameters (for example, thousands or millions) can be optimized on a training set, where the desired output is known. The problem is typically nonconvex and plagued by over-fitting problems, and so advanced methods are necessary in order to get reliable answers. One tool that has been exploited is principal component analysis (PCA), which reduces the dimensionality of the data to the most important “directions.” Immediately the practitioner of renormalization group (RG) methods recognizes an analogy, since the RG techniques are also supposed to identify the most important directions in an enlarged space of Hamiltonians. One of the motivations of the present research is to make this analogy more concrete.

A number of papers [1–3] attempt to draw a connection between deep learning and the RG as it appears in physics. However, the analogies between RG flow and depth in a neural network would be strengthened if one could determine conditions under which fixed points can be identified. It would be helpful to show more explicitly how passing from one level to another in a neural

network genuinely translates to a renormalization group transformation. There have been steps in the direction of making a full connection. For instance in [2], the principle of *causal influence* is emphasized. That is, when descending in depth, only neighboring nodes should influence the outcome of a lower level node. We have also implemented this in a simple training scheme in earlier work [4]. It can be called “cheap learning” because far fewer variational parameters are involved, due to the constraints of locality. In [3] it is emphasized that deep neural networks outperform shallower networks for reasons which may ultimately be understood in terms of the power of the renormalization group. Other topics related to machine learning, such as principal component analysis [5] have been previously interpreted in terms of the renormalization group (in this case momentum shells). Machine learning has also been used to identify phase transitions in numerical simulations [6–9].

RG transformations are usually defined in a space of couplings/Hamiltonians, but typically, it is not possible to write down Hamiltonians directly associated with images sets. In this article we propose RG transformations that can be applied to a specific set of images but which could be generalized for other image sets, and can also be understood analytically without any graphical representation. We use the well-studied example of the two-dimensional Ising model on a square lattice. The spin configurations generated with importance sampling provide images with black and white pixels. They have features that can be used to attempt to recognize the temperature used to generate them. However, constructing blocked Hamiltonians in configuration space is a difficult task which involves approximations that are difficult to

* samuel-foreman@uiowa.edu

† giedtj@rpi.edu

‡ yannick-meurice@uiowa.edu

§ jfunmuth@syr.edu

improve. In other words, it is very difficult to explicitly construct the exact RG transformation mapping the original couplings among the Ising spins into coarse grained ones.

A better control on the RG transformation can be achieved by using the tensor renormalization group (TRG) method [10–16]. The starting point for this reformulation is the character expansion of the Boltzmann weights which is also used in the duality transformation [17]. This leads to an exact expression of the partition function as a sum over closed paths which can be generated with importance sampling using the worm algorithm [18] and then pixelated. These samples will be our sets of images indexed by the temperature used to generate them. The procedure is reviewed in Sec. II.

The goal of a RG analysis is to study systems with large correlation lengths in lattice spacing units and iteratively replace them by coarser ones with a larger effective lattice spacing. This process is useful if we can tune a parameter such as the temperature towards its critical value. Typical image sets such as the MNIST data can be thought as “far from criticality” and the use of RG methods for such a data set may be of limited interest [4]. Criticality may sometimes refer to the choice of parameters used in data analysis [19]. It seems crucial to introduce a systematic way to deal with the concept of criticality in ML.

The PCA is a standard method to analyze sets of images. In configuration space, the PCA analysis is identical to the study of the spin-spin correlation matrix. In particular, the largest eigenvalue λ_{max} is directly connected to the magnetic susceptibility which diverges at criticality [7]. In the loop representation (worms), we will show that λ_{max} diverges logarithmically at criticality with a constant of proportionality which can be estimated quite precisely ($3/\pi$). This is explained in Sec. III. More generally, it seems reasonable to identify the criticality with the divergence of λ_{max} .

The advantage of rewriting the high-temperature expansion in terms of tensors is that it allows a very simple blocking (coarse-graining) procedure where a group of sites is replaced by a single site. In the TRG approach the blocking procedure is local. This leads to simple and exact coarse-graining formulas because we can separate the links into two categories: those links that are inside the blocks and integrated over, and those outside the blocks which are kept fixed and communicate between the blocks [13]. The main goal of this article is to relate blocking procedures that can be applied to sets of pixelated images, to approximate TRG transformations. A short summary of the TRG procedure is given in Sec. IV.

Having defined criticality, the next step is to define a RG transformation for sets of “legal” loop configurations, also called “worm configurations” later, sampled at various temperatures. In Sec. V, we propose a family of transformations which replaces two parallel links in a block by a single link carrying a specific value x . We call this procedure $1+1 \rightarrow x$ hereafter. In the case $1+1 \rightarrow 0$,

the blocked images follow the same rules (for legal configurations) as the original ones. There is a clear analogy with the 2-state approximation of the TRG method. In the 2-state TRG approximation, the average fraction of occupied links shows a characteristic crossing at a critical point and a collapse when the distance to the critical point is appropriately rescaled at each iteration. The average fraction of occupied links in the blocked worm configurations (with $1+1 \rightarrow 0$) shows a somewhat similar behavior in the low temperature phase. However, on the high-temperature side, we observe a “merging” rather than a crossing. In Sec. VI, we provide explanations for the similarities and differences between the two procedures.

In Sec. VII we discuss an approximate 2-state TRG method to calculate the average number of bonds through several iterations. The worm configurations can be directly connected to spin configurations using duality [17]: they are the boundary of the positive spin islands. This suggests that the methods discussed here could be applied to generic images. Boundaries of generic grayscale pictures can be defined by converting the picture to black and white pixels. A grayscale picture with gray values between 0 and 1 can be converted into an Ising spin configuration, by introducing a “graycut” below which the value is converted to 0 (spin down) and above which the value is converted to 1 (spin up). It is then possible to construct the boundaries of the spin up domains. This is illustrated in Fig. 1. Possible applications are briefly discussed in the Conclusions and illustrated with the CIFAR database in Appendix B.

II. FROM LOOPS TO IMAGES

In the following we consider the two-dimensional Ising model with spins $\sigma_i = \pm 1$ on a square lattice. The partition function reads

$$Z = \sum_{\{\sigma_i\}} e^{\beta \sum_{\langle i,j \rangle} \sigma_i \sigma_j}, \quad (1)$$

where $\langle i,j \rangle$ denotes nearest neighbor sites on the square lattice. In some occasions we will use the notation $T = 1/\beta$ for the temperature. The partition function can be rewritten by using the character expansion [17]

$$\exp(\beta\sigma) = \cosh(\beta) + \sigma \sinh(\beta), \quad (2)$$

and integrating over the spins. Factoring out the $\cosh(\beta)$, each link can carry a weight 1 when unoccupied or $t \equiv \tanh(\beta)$ when occupied. The integration over the spins guarantees that an even number of occupied links is coming out of each site [17]. The set of occupied links then form a “legal graph” with N_b occupied links. The partition function can then be written as sum over such legal graphs. If $\mathcal{N}(N_b)$ denotes the number of legal graphs with N_b links we can write:

$$Z = 2^V (\cosh(\beta))^{2V} \sum_{N_b} t^{N_b} \mathcal{N}(N_b). \quad (3)$$

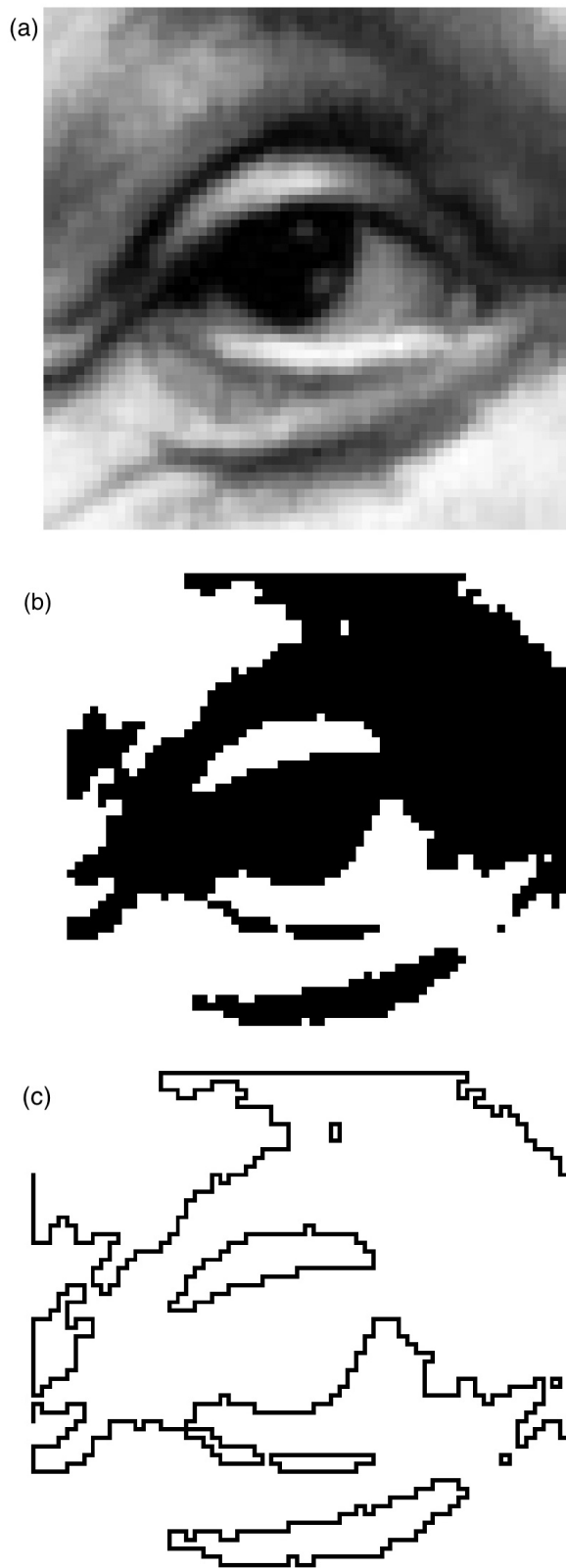


FIG. 1. (a) Picture of an eye with 4096 pixels; (b) black and white version with a graycut at 0.72; (c) boundaries of the black domains.

Using the fact that $\tanh(\beta) = \exp(-2\tilde{\beta})$, with $\tilde{\beta}$ the inverse dual temperature, Eq. (3) has the same form as a spectral decomposition using a density of states and a Boltzmann weight (with $2N_b$ playing the role of the energy). Details of this reformulation can be found in Appendix A 1.

As shown in Appendix A 2, we can use derivatives of the logarithm of the partition function to relate $\langle N_b \rangle$ to the average energy, and the bond number fluctuations,

$$\langle \Delta_{N_b}^2 \rangle \equiv \langle (N_b - \langle N_b \rangle)^2 \rangle, \quad (4)$$

to the specific heat per site. From the logarithmic singularity of the specific heat we find that

$$\langle \Delta_{N_b}^2 \rangle / V = -\frac{2}{\pi} \ln(|T - T_c|) + \text{regular}. \quad (5)$$

In the following we use interchangeably the “bond” terminology, for instance in N_b as in [18] and the link terminology more common in the lattice gauge theory context. In all our numerical simulations we use periodic boundary conditions which guarantees translation invariance.

We will show in Sec. IV that the new form of the partition function in Eq. (3) can also be written in an equivalent way as a sum of products of tensors with four indices contracted along the links of the lattice.

The contributions to Eq. (3) can be sampled using a worm algorithm [18] outlined in Appendix A 3. Using this algorithm, we generated multiple configurations at each temperature ($N_{\text{configs}} \approx 10,000$) which are then used for averaging. For example, we can calculate the average number of occupied bonds at a particular temperature by averaging over all configurations.

Using a legal graph (worm configuration), we can construct an image by introducing a lattice of $2L \times 2L$ pixels with a size of one half lattice spacing. One quarter of these pixels are attached to the sites, one quarter to the horizontal links and one quarter to the vertical links. The remaining quarter are in the middle of the plaquettes and always white. In this representation, each site, link, and plaquette are designated an individual pixel, where occupied links and their respective endpoints are colored black. An example of this representation is shown in Fig. 2. We can then flatten each of these images into a vector $\mathbf{v} \in \mathbb{R}^{4V}$, with $v_i \in \{0, 1\}$. This allows us to write the number of occupied bonds, in a single configuration, N_b as

$$\sum_{j=\text{bonds}} v_j = N_b \quad (6)$$

III. PCA AND CRITICALITY

Having now sets of images for a range of temperatures, we can apply PCA [20]. PCA isolates the “most relevant” directions in the dataset. PCA is simply the computation of the eigenvalues λ_α and eigenvectors u_α of the

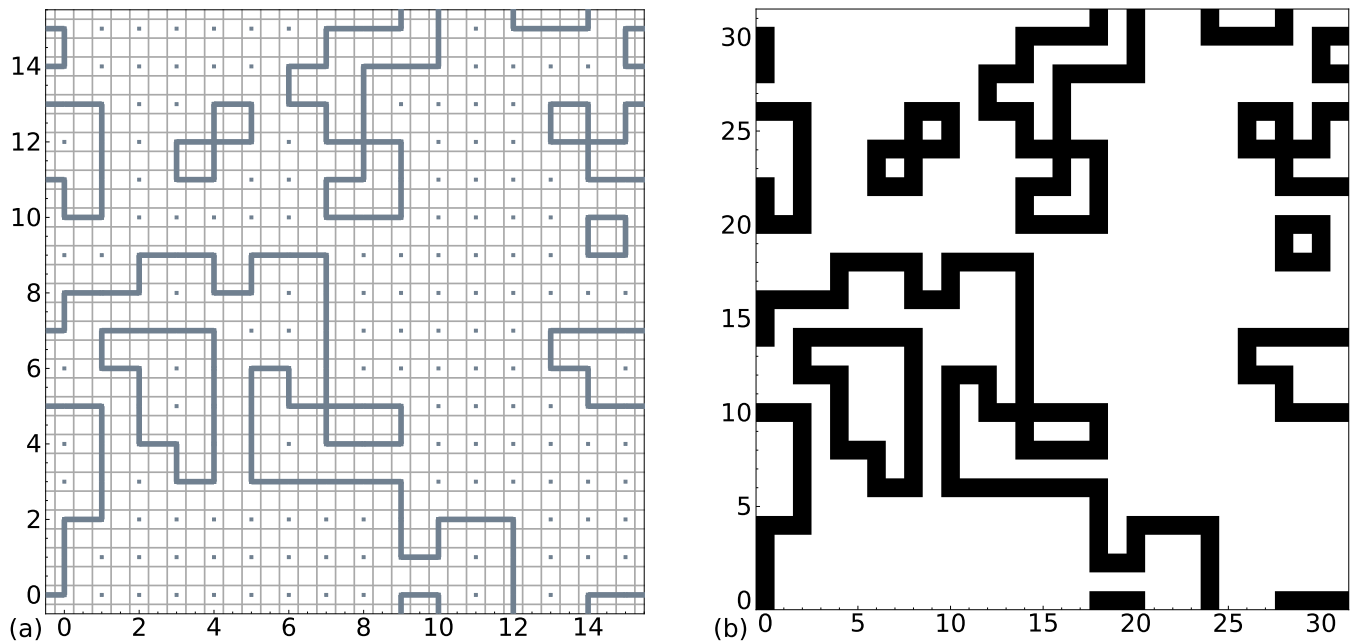


FIG. 2. (a) Legal worm configuration on an $L \times L$ lattice with periodic boundary conditions and; (b) its equivalent representation as a $2L \times 2L$ black and white pixel image.

covariance matrix for a dataset with N configurations corresponding to a given temperature $\{\mathbf{v}^n\}_{n=1}^N$:

$$S_{ij} = \frac{1}{N} \sum_{n=1}^N (v_i^n - \bar{v}_i)(v_j^n - \bar{v}_j). \quad (7)$$

In this equation, each sample \mathbf{v}_j is a vector in \mathbb{R}^{4V} , labeled by the indices $i, j = 1, \dots, 4V$. The PCA extracts solutions to

$$S u_\alpha = \lambda_\alpha u_\alpha \quad (8)$$

and orders them, in descending magnitude of λ_α , which are all non-negative. The usefulness of PCA is that one can approximate the data (see for instance the discussion in [20]) by the first M principal components.

Illustrations of the PCA for the MNIST data can be found in Sec. 4 of Ref. [4], where we show the eigenvectors corresponding to the largest eigenvalues and the approximation of the data by subspaces of the largest eigenvalues of dimensions 10, 20 etc.

It should be noted that the PCA is an analysis that can be performed for each temperature separately and not obviously connected to the closeness to criticality. However, we were able to find a relation between the largest PCA eigenvalue denoted λ_{max} and the logarithmic divergence of the specific heat, namely

$$\lambda_{max} \simeq \frac{3}{2} \langle \Delta_{N_b}^2 \rangle / V \simeq -\frac{3}{\pi} \ln(|T - T_c|). \quad (9)$$

This property was found by an approximate reasoning shown in Appendix A 2 and relies on two assumptions.

The first one is that the eigenvector associated with λ_{max} is proportional to $\langle \mathbf{v} \rangle$ which is invariant under translation by two pixels in either direction. The second assumption is that in good approximation we can neglect the contributions from sites that are visited twice (four occupied links coming out of one site). Numerically, only 4% of sites are visited twice near the critical temperature which justifies the second assumption. Figure 3 provides an independent confirmation of the approximate validity of Eq. (9).

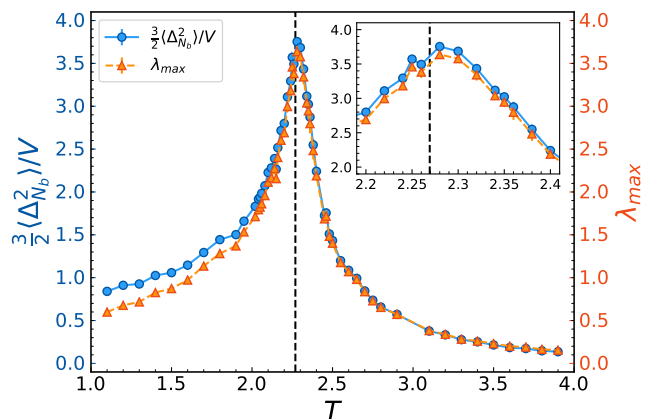


FIG. 3. λ_{max} and $\frac{3}{2} \langle \Delta_{N_b}^2 \rangle / V$ (per unit volume) vs. T , illustrating the relation between the eigenvalue corresponding to the first principal component and the logarithmic divergence of the specific heat. The inset shows a qualitative agreement near the critical temperature.

IV. TRG COARSE-GRAINING

So far we have sampled the legal graphs of the high temperature expansion of the Ising model using the worm algorithm. An alternative approach is to use a tractable real-space renormalization group method known as the TRG [12–16].

In order to understand what we want to accomplish by blocking the loop configuration, it is useful to first understand the evolution of a tensor element using the TRG method.

The tensor formulation used here connects easily with the worm formulation used in this paper. After the character expansion has been carried out, one is left with new integer variables on the links of the lattice with constraints on the sites which guarantee the sum of the link variables associated with that site is even. Therefore we build a tensor using this constraint and the surrounding link weights. The tensor has the form

$$T_{xx'yy'}^{(i)}(\beta) = [\tanh(\beta)]^{(n_x+n_{x'}+n_y+n_{y'})/2} \times \delta_{n_x+n_{x'}+n_y+n_{y'},0 \bmod 2}. \quad (10)$$

Here the notation being used is that this tensor is located at the i^{th} site of the lattice, $n_{\hat{\mu}}$ is the integer variable, taking value 0 or 1, on an adjacent link, and the Kronecker delta, $\delta_{i,j}$ is understood to be satisfied if the sum is even. By contracting these tensors together in the pattern of the lattice one recreates the closed-loop paths generated by the high-temperature expansion and exactly match those paths which are sampled by the worm algorithm.

Using these tensors one can write a partition function for the Ising model that is exactly equal to the original partition function,

$$Z = 2^V (\cosh(\beta))^{2V} \text{Tr} \prod_i T_{xx'yy'}^{(i)} \quad (11)$$

where Tr means contractions (sums over 0 and 1) over the links.

The most important aspect of this reformulation is that it can be coarse-grained efficiently. The process is illustrated in Fig. 4 where four fundamental tensors have been contracted to form a new “blocked” tensor. This new tensor has a squared number of degrees of freedom for each new effective index. The partition function can be written exactly as

$$Z = 2^V (\cosh(\beta))^{2V} \text{Tr} \prod_{2i} T_{XX'YY'}^{(2i)},$$

where $2i$ denotes the sites of the coarser lattice with twice the lattice spacing of the original lattice. In practice, this exact procedure cannot be repeated indefinitely and truncations are necessary. This can be accomplished by projecting the product states into a smaller number of states that optimizes the closeness to the exact answer. A two-state projection is discussed in [13] and will be followed hereafter. Note that in this procedure, T_{0000} is factored

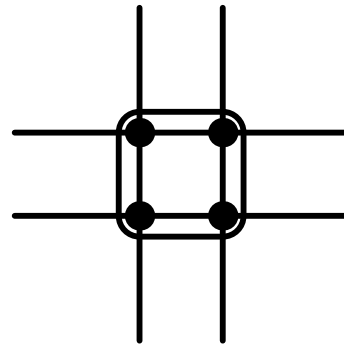


FIG. 4. Illustration of the tensor blocking discussed in the text. Each dot is a tensor at a lattice site with four lines coming out, each representing a tensor index. Lines connecting dots represent tensor contractions.

out and the final expression for the other blocked tensors are given in these units. For definiteness we consider T_{1100} which in the microscopic formulation is the weight associated with a horizontal line in a loop configuration. By looking at the fixed point equation [13], one can see that there is a high temperature fixed point where all the tensor elements except for T_{0000} are zero and a low temperature fixed point where all the tensor elements are one. In between these two limits, there is a non-trivial fixed point illustrated by the crossing of iterated values of T_{1100} in Fig. 5. Note that because of the two-state approximation, the critical temperature T_c is slightly higher than the exact one [13]. To be completely specific, the exact T_c for the original model is $2/\ln(1+\sqrt{2}) = 2.269\dots$ while for the two state projection with the second projection procedure of Ref. [13], it is $1/0.3948678 = 2.53249\dots$

It is easy to relate the properties of the iterated curves near the non-trivial fixed point using the linear RG approximation. Below we just state the results, for details and references see [13]. With the blocking procedure used, the scale factor is $b = 2$. The eigenvalue in the relevant direction is $\lambda = b^{1/\nu} = 2$ since $\nu = 1$. In Fig. 5(a), one can see that the height

$$\delta T_{1100} \equiv T_{1100} - T_{1100}^* \quad (12)$$

(where T_{1100}^* is the value at the fixed point), nearly doubles each time the blocking procedure is performed, making the slope twice as large each time. A nice data collapse can be reached by offsetting this effect by rescaling the horizontal axis each iteration by $\lambda=2$ as shown in Fig. 5(b). In numerical calculations, we start with a finite L (64 in Fig. 5) and then after ℓ iterations, we are left with an effective size $L_{eff} = L/b^\ell$.

The remainder of the paper will be dedicated towards obtaining data collapse for $\langle N_b \rangle$ calculated with successive blockings.

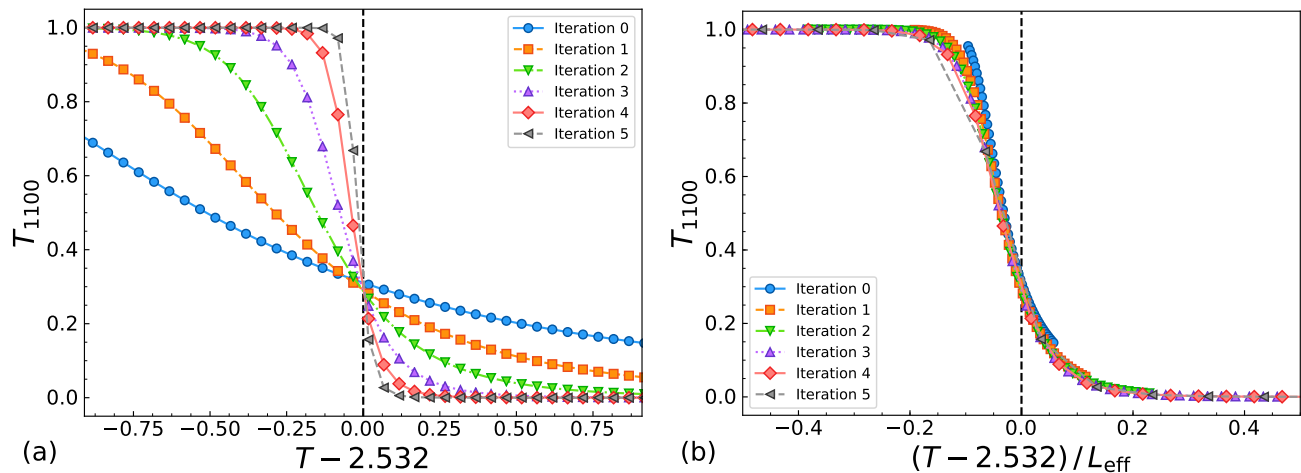


FIG. 5. (a) T_{1100} vs. $T - T_c^{(2s)}$ for six successive iterations of the blocking transformation, beginning with an initial lattice $L = 64$; (b) T_{1100} vs. $(T - T_c^{(2s)})/L_{\text{eff}}$ illustrating the data collapse, where $T_c^{(2s)}$ is the critical temperature of the two state projection, beginning at iteration 0 on an $L = 64$ lattice.

V. IMAGE COARSE-GRAINING

In an attempt to explicitly connect the ideas from RG theory to similar concepts in machine learning, we will implement a coarse-graining procedure directly on the images but in a way inspired by the TRG construction of Sec. IV. The construction relies on visual intuition and will be reanalyzed in the TRG context in Sec. VII.

As in the TRG coarse-graining procedure, the image is first divided up into blocks of 2×2 squares, as shown in Fig. 6. Each of these 2×2 squares are then replaced,

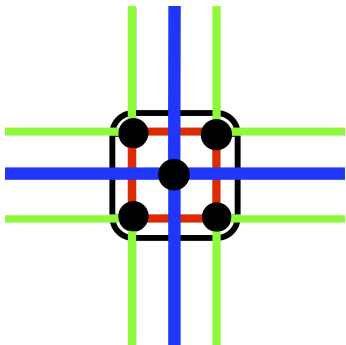


FIG. 6. Illustration of an elementary block in the image coarse-graining procedure consisting of four sites, four internal bonds (red), eight external bonds (green), and four blocked external bonds (blue).

or “blocked”, by a single site with bonds determined by the number of occupied external bonds in the original square. In doing so, we reduce the size of each linear dimension by a factor of two, resulting in a new blocked configuration whose volume is one-quarter the original. In particular, if a given block has exactly one external bond in a given direction, the blocked site retains this bond in the blocked configuration. This seems to be a

natural choice. However, if a given block has exactly two external bonds in a given direction, we can consider several options. The simplest option is to neglect the double bond entirely, and we denote this blocking scheme by “ $1 + 1 \rightarrow 0$ ”. This approach respects the selection rule (conservation modulo 2) and has the advantage of maintaining the closed-path restriction. In other words with the $1 + 1 \rightarrow 0$ option, the blocked image corresponds to a legal graph and the procedure can be iterated without introducing new parameters. This procedure is illustrated for a specific configuration on a 16×16 lattice in Fig. 7.

Alternatively, we can include this double bond in the blocked configuration, and give it some weight m between 0 and 2. The examples of $m = 1$ and 2 are denoted “ $1 + 1 \rightarrow 1$ ”, and “ $1 + 1 \rightarrow 2$ ” respectively and are shown in Fig. 16. This blocking procedure introduces new elements and iterations require more involved procedures. This is not discussed hereafter.

VI. PARTIAL DATA COLLAPSE FOR BLOCKED IMAGES

In this section, we study the properties of $\langle N_b \rangle$ obtained for successive blockings with the $1 + 1 \rightarrow 0$ rule starting with configurations on a 64×64 lattice. A first observation is that the $1 + 1 \rightarrow 0$ blocking preserves the location of the peak of the fluctuations $\langle \Delta_{N_b}^2 \rangle$. In addition it is possible to stabilize this quantity for a few iterations by dividing by $V_{\text{eff}} \ln(L_{\text{eff}})$. This is illustrated in Fig. 8. However, a very different scaling appears for the last two iterations which may be due to the very short effective sizes (4 and 2). This indicates the last two iterations are very different from the previous ones.

We now consider $\langle N_b \rangle$ for successive iterations. The results are shown in Fig. 9. We see that in the low tem-

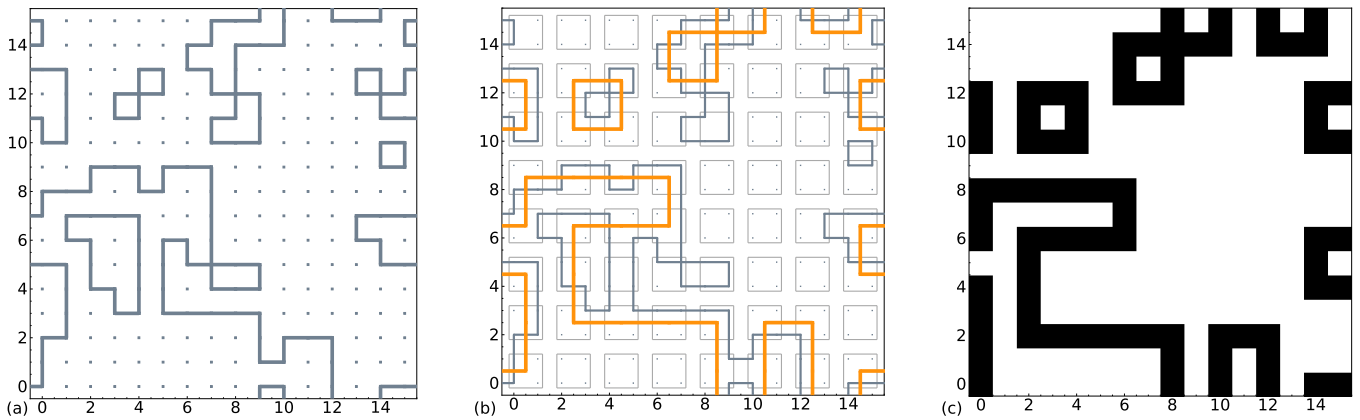


FIG. 7. (a) Illustration of the $1 + 1 \rightarrow 0$ blocking procedure discussed in the text: original configuration; (b) introduction of the blocks and replacement of single or double bounds according to the $1 + 1 \rightarrow 0$ rule; (c) construction of the corresponding blocked image.

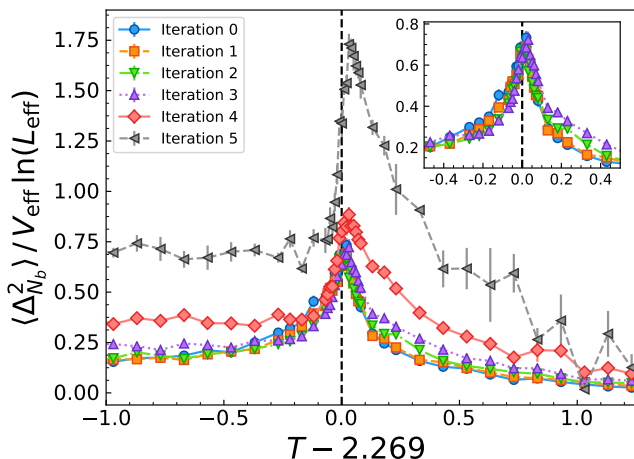


FIG. 8. Fluctuations in the average number of bonds $\langle \Delta_{N_b}^2 \rangle$ vs. temperature T under iterated blocking steps beginning with an initial lattice size of $L = 64$. The results are scaled by $1/V_{\text{eff}} \log(L_{\text{eff}})$ in order to demonstrate the data collapse near the critical temperature. This collapse is especially apparent in the inset, which shows the results under the first three blocking steps, with $L_{\text{eff}} = 64, 32, 16$, and 8 .

perature side, the curves sharpen in a way similar to T_{1100} in Fig. 5. However on the high temperature side, we observe a merging rather than a crossing. This can be explained as follows. In the high T regime occasionally a single loop, the size of a plaquette, forms. This is due to other configurations being highly suppressed. With the $1 + 1 \rightarrow 0$ rule, one out of four possible plaquettes becomes a larger plaquette which exactly compensates the change in V_{eff} which is also reduced by a factor of four. There are four kinds of plaquettes (see Fig. 7): those inside the blocks (they disappear after blocking), those between two neighboring blocks in the vertical or horizontal direction (these are double links between the blocks and so they disappear with the $1 + 1 \rightarrow 0$ rule),

and finally those which share a corner with four blocks (they generate a larger plaquette). This last type can be seen at coordinate $(4, 12)$ in Fig. 7.

We now attempt to obtain data collapse for $\langle N_b \rangle / V_{\text{eff}}$ by performing a rescaling of the temperature axis with respect to the critical value as in Fig. 5. After this rescaling by a factor 2 at each iteration, we observe a reasonable collapse on the low-temperature side. On the high temperature side, since the unrescaled curves merge, the rescaling splits them and there is no collapse on that side. This is illustrated in Fig. 9.

VII. TRG CALCULATION OF $\langle N_b \rangle$

Using the tensor method we were able to calculate $\langle N_b \rangle$ to compare with the worm algorithm. Consider the equation for $\langle N_b \rangle$ with $N_b = \sum_l n_l$ the sum over bond numbers at every link:

$$\langle N_b \rangle = \frac{1}{Z} \sum_{\{n\}} \left(\sum_l n_l \right) \left(\prod_l \tanh^{n_l}(\beta) \right) \times \left(\prod_i \delta_{n_x + n_{x'} + n_y + n_{y'}, 0 \pmod{2}}^{(i)} \right). \quad (13)$$

This expression can be seen as $\langle N_b \rangle = \sum_l \langle n_l \rangle$, and because of translation and 90° rotational invariance, all $\langle n_l \rangle$ are equal. Thus, it is enough to calculate $\langle n_l \rangle$ for one particular link (just call it $\langle n \rangle$) and multiply it by $2V$: $\langle N_b \rangle = 2V \langle n \rangle$.

To calculate $\langle n \rangle$, it amounts to associating an n with one particular link on the lattice. This alters *two* tensors on the lattice such that the two tensors which contain that link as indices are now defined as

$$\tilde{T}_{n_x n_{x'} n_y n_{y'}}^{(1)} = \sqrt{n_x} T_{n_x n_{x'} n_y n_{y'}}(\beta), \quad (14)$$

$$\tilde{T}_{n_x n_{x'} n_y n_{y'}}^{(2)} = \sqrt{n_{x'}} T_{n_x n_{x'} n_y n_{y'}}(\beta), \quad (15)$$

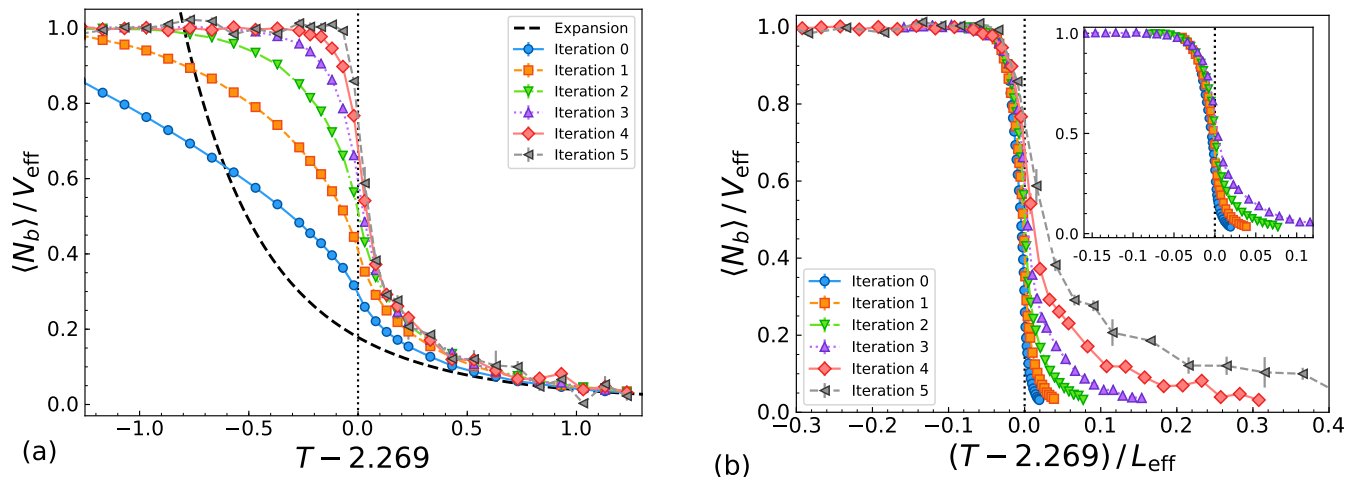


FIG. 9. (a) Average number of bonds $\langle N_b \rangle$ vs. temperature T under iterated blocking steps beginning with an initial lattice size of $L = 64$. The dashed black line illustrates the high temperature expansion, showing that the dominant configurations are those consisting of small, isolated plaquettes. (b) Average number of bonds $\langle N_b \rangle$ vs. the rescaled temperature $(T - 2.269) / L_{\text{eff}}$ under successive blocking steps. Iteration 0 represents the original lattice before blocking, with $L_{\text{eff}} = 64$.

where x and x' were chosen without loss of generality. It could just as well have been chosen as y and y' . One can see that when these two tensors are contracted along their shared link, the product picks up a factor of n for that link, which when combined with the other tensors in the lattice, and divided by Z , yields $\langle n \rangle$.

Knowing the above, one is free to block and construct the partition function, Z , and $\langle n \rangle$. This can be done by blocking symmetrically in both directions, or by constructing a transfer matrix by contracting only along a time-slice (i.e. a snapshot of the system at fixed t). This is shown in Fig. 10. In practice contracting to build a transfer matrix is optimum since one direction of the lattice is never renormalized and allows the easy calculation of $\langle n \rangle$. What was just described is a method to calculate

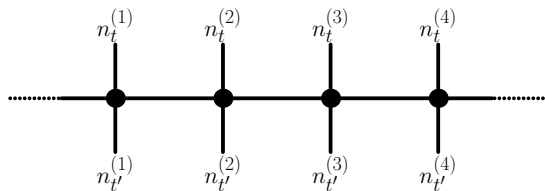


FIG. 10. A pictorial representation of the transfer matrix made by contracting a fundamental tensor along a single time-slice.

$\langle n \rangle$ for the original, fine lattice. However, one can also calculate the same quantity for a coarse lattice. The actual blocking method is essentially identical, with a small difference. Instead of contracting the fundamental tensor to the desired lattice size, one contracts a blocked tensor to the desired lattice size.

For example, if one wanted to calculate $\langle N_b \rangle$ for a 32×32 lattice, one could contract the fundamental tensor along a time slice with itself five times. This would

give a $2^{32} \times 2^{32}$ transfer matrix which could be used to build the whole partition function. Now, under a single coarse-graining step the 32×32 lattice becomes a 16×16 lattice of blocks. Therefore, to build this, one could contract four fundamental tensors in a block and consider this a new, effective fundamental tensor. This is shown in Fig. 4. Then one repeats the same steps to construct the transfer matrix, however only contracting four times with itself to create a matrix representing 16 lattice sites of the blocked tensor.

To actually calculate $\langle n \rangle$ by building the transfer matrix, one can take the final tensor, prior to contracting the dangling spatial indices, and multiply by \sqrt{n} against the indices n_x and $n_{x'}$. This is shown in Fig. 11, however the procedure is identical for the blocked case once the blocked tensor has been constructed. This is also the point where one can choose

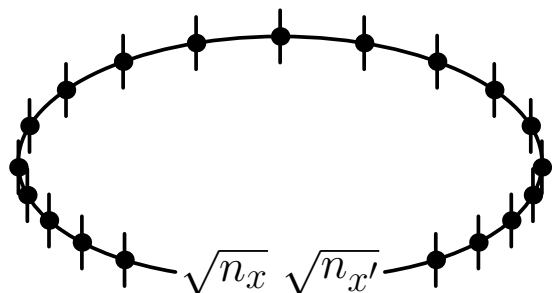


FIG. 11. By multiplying the remaining free spatial indices by \sqrt{n} and contracting for periodic boundary conditions in space we form an “impure” transfer matrix. Combining the resultant matrix with the original transfer matrix allows one to calculate $\langle n \rangle$.

the level of approximation one will use in the blocking. For instance one could choose that the state $|1\ 1\rangle \rightarrow |0\rangle$

and assign $n = 0$ to that state. Alternatively one could preserve N_b and let $|1\ 1\rangle \rightarrow |2\rangle$ and assign $n = 2$ to that state. This procedure was found to agree with the results obtained by changing the pixels of the worm configurations.

Once the original transfer matrix has been constructed, as well as the matrix with the insertion of n along a single link, one can combine these to find $\langle n \rangle$. This is done by simple matrix multiplication:

$$\langle n \rangle = \frac{1}{Z} \text{Tr} \left[\underbrace{\mathbb{T} \cdots \mathbb{T}' \cdots \mathbb{T}}_{N_\tau} \right], \quad (16)$$

with

$$Z = \text{Tr} [\mathbb{T}^{N_\tau}]. \quad (17)$$

Here \mathbb{T} represents the transfer matrix built by contracting tensors along a time slice, and \mathbb{T}' represents the single (“impure”) transfer matrix at a time-slice with a single bond multiplied by n . Since the lattice has Euclidean temporal extent, $L = N_\tau$, there are that many matrices multiplied in each case. The values of $\langle N_b \rangle / V_{eff}$ obtained with this procedure are shown in Fig. 12. The rescaling by 2 at each iteration provides a good data collapse on both sides of the transition.

VIII. CONCLUSIONS

In summary, we have motivated, constructed and applied a RG transformation to sets of worm configurations at various temperature. This transformation is approximate and the coarse-grained configurations are themselves worm configurations. This allows multiple iterations. We monitored the bond density at successive iterations and compared them with a two-state TRG approximation. We found clear similarities in the low-temperature side, where data collapse is observed for both procedures when the distance to the critical point is rescaled at each iteration. In the high-temperature phase, only the TRG approximation shows good data collapse.

Can the procedure developed here be applied to the boundary of arbitrary sets of images as illustrated in the introduction? The gray cutoff could be used as a tunable parameter. However, in the limiting cases of a zero (one) gray cutoff we have uniform black (white) images which are both similar to the high-temperature phase, and we do not expect a phase transition. Applications to the CIFAR dataset are discussed in Appendix B and confirm this point of view.

RG methods have been considered for assisting in image recognition [21–23]. By mapping from fine to coarse in several ways, such as the $1+1 \rightarrow 0$ and $1+1 \rightarrow 1$ in our approach, one begins to see how the inverse process might go in replacing a degraded image with a higher resolution reconstruction. The physics of defining RG transformations and quantifying scheme dependence then guides

such reconstructions using physical principles, which are expected to be embedded into real world image characteristics due to principles of universality.

It should be noted that the TRG procedure is often considered as a “local update“ of the tensor. A more sophisticated approach consists of using the standard recursion to provide an environment for subsequent updates [12, 24]. An environment tensor E is propagated backward from the coarse to the fine scale. An improved version of the initial iteration can then be performed in an environment. This forward-backward procedure can be repeated and is very reminiscent of the procedure proposed by Hinton and Salakhutdinov [25] in the context of image recognition.

A better understanding of RG concepts in machine learning could enhance physics discovery, especially in the context of simulation and modeling of physical systems at a fundamental level [26]. The general idea is to render computational tools “smart,” i.e., that they would learn features and patterns without the intervention of a human “assistant,” and would, in the best possible scenario, guide the direction of further simulations. This could accelerate and deepen the process of understanding and characterizing the complex systems that are deemed important in pure and applied physics.

ACKNOWLEDGEMENTS

This research was supported in part by the Department of Energy, Office of Science, Office of High Energy Physics, Grant No. DE-SC0013496 (JG) DE-SC0010113 (YM) and DE-SC0009998 (JUY) and Office of Workforce Development for Teachers and Scientists, Office of Science Graduate Student Research (SCGSR) program. The SCGSR program is administered by the Oak Ridge Institute for Science and Education (ORISE) for the DOE. ORISE is managed by ORAU under contract number DESC0014664 (SF).

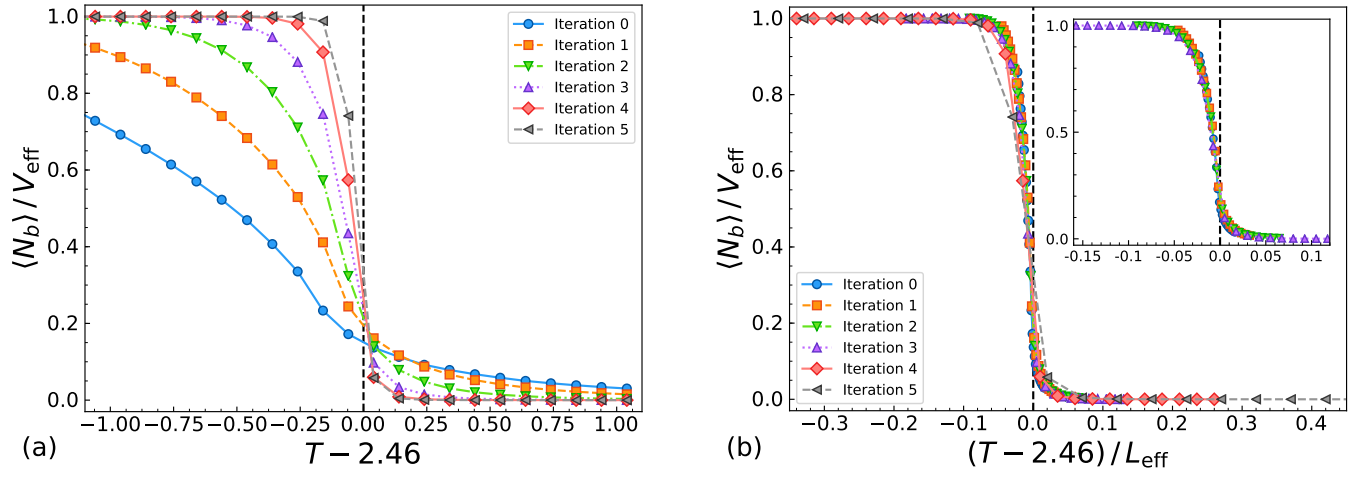


FIG. 12. (a) $\langle N_b \rangle$ vs $(T - 2.46)$ under successive blocking steps calculated using 2-state HOTRG. (b) $\langle N_b \rangle$ vs $(T - 2.46) / L_{\text{eff}}$ under successive blocking steps calculated using 2-state HOTRG. Note that the value of 2.46 was determined qualitatively by choosing the value which gave the best resulting data collapse.

-
- [1] S.-H. Li and L. Wang, [1802.02840](#).
 - [2] C. Béný, [arXiv:1301.3124](#).
 - [3] P. Mehta and D. J. Schwab, [arXiv:1410.3831](#).
 - [4] S. Foreman, J. Giedt, Y. Meurice, and J. Unmuth-Yockey, *Proceedings, 35th International Symposium on Lattice Field Theory (Lattice 2017): Granada, Spain, June 18-24, 2017*, *EPJ Web Conf.* **175**, 11025 (2018), [arXiv:1710.02079 \[hep-lat\]](#).
 - [5] S. Bradde and W. Bialek, *Journal of Statistical Physics* **167**, 462, [arXiv:1610.09733](#).
 - [6] J. Carrasquilla and R. G. Melko, *Nature Physics* **13**, 431 (2017), [arXiv:1605.01735 \[cond-mat.str-el\]](#).
 - [7] L. Wang, *Phys. Rev. B* **94**, 195105 (2016).
 - [8] W. Hu, R. R. P. Singh, and R. T. Scalettar, *Phys. Rev. E* **95**, 062122 (2017), [arXiv:1704.00080 \[cond-mat.stat-mech\]](#).
 - [9] S. J. Wetzel, *Phys. Rev. E* **96**, 022140 (2017), [arXiv:1703.02435 \[cond-mat.stat-mech\]](#).
 - [10] M. Levin and C. P. Nave, *Phys. Rev. Lett.* **99**, 120601 (2007).
 - [11] Z.-C. Gu, M. Levin, B. Swingle, and X.-G. Wen, *Phys. Rev. B* **79**, 085118 (2009).
 - [12] Z. Y. Xie, J. Chen, M. P. Qin, J. W. Zhu, L. P. Yang, and T. Xiang, *Phys. Rev. B* **86**, 045139 (2012).
 - [13] Y. Meurice, *Phys. Rev.* **B87**, 064422 (2013), [arXiv:1211.3675 \[hep-lat\]](#).
 - [14] Y. Liu, Y. Meurice, M. P. Qin, J. Unmuth-Yockey, T. Xiang, Z. Y. Xie, J. F. Yu, and H. Zou, *Phys. Rev.* **D88**, 056005 (2013), [arXiv:1307.6543 \[hep-lat\]](#).
 - [15] A. Denbleyker, Y. Liu, Y. Meurice, M. P. Qin, T. Xiang, Z. Y. Xie, J. F. Yu, and H. Zou, *Phys. Rev.* **D89**, 016008 (2014), [arXiv:1309.6623 \[hep-lat\]](#).
 - [16] J. F. Yu, Z. Y. Xie, Y. Meurice, Y. Liu, A. Denbleyker, H. Zou, M. P. Qin, and J. Chen, *Phys. Rev.* **E89**, 013308 (2014), [arXiv:1309.4963 \[cond-mat.stat-mech\]](#).
 - [17] R. Savit, *Rev. Mod. Phys.* **52**, 453 (1980).
 - [18] N. Prokof'ev and B. Svistunov, *Phys. Rev. Lett.* **87**, 160601 (2001).
 - [19] T. A. Enßlin and M. Frommert, *Phys. Rev. D* **83**, 105014 (2011).
 - [20] C. M. Bishop, *Pattern recognition and machine learning* (Springer, New York, 2006).
 - [21] B. Gidas, *IEEE Transactions on Pattern Analysis and Machine Intelligence* **11**, 164 (1989).
 - [22] K. Tanaka, *Journal of Physics A: Mathematical and General* **35**, R81 (2002).
 - [23] T. Horiguchi, Y. Honda, and M. Miya, *Physics Letters A* **227**, 319 (1997).
 - [24] Z. Y. Xie, H. C. Jiang, Q. N. Chen, Z. Y. Weng, and T. Xiang, *Phys. Rev. Lett.* **103**, 160601 (2009).
 - [25] G. E. Hinton and R. R. Salakhutdinov, *Science* **313**, 504 (2006), <http://science.sciencemag.org/content/313/5786/504.full.pdf>.
 - [26] P. E. Shanahan, D. Trewartha, and W. Detmold, *Phys. Rev.* **D97**, 094506 (2018), [arXiv:1801.05784 \[hep-lat\]](#).
 - [27] R. H. Swendsen and J.-S. Wang, *Phys. Rev. Lett.* **58**, 86 (1987).
 - [28] B. Kaufman, *Phys. Rev.* **76**, 1232 (1949).
 - [29] A. Krizhevsky and G. Hinton, Master's thesis, Department of Computer Science, University of Toronto (2009).

Appendix A: Technical results

1. Loop representation

We can rewrite the Ising partition function in terms of bonds between neighboring sites $\langle i, j \rangle$. The allowed bond configurations are concisely described by concepts in graph theory, because they form edges (bonds) between neighboring vertices (sites). Making use of well-known identities allows for the partition function to be written in the following high-temperature expansion:

$$Z = 2^{|V|} \cosh^{|E|} \beta \sum_{\Gamma \in \mathcal{C}(G)} \tanh^{|\Gamma|} \beta \quad (\text{A1})$$

$$= 2^{|V|} \cosh^{|E|} \beta \sum_{|\Gamma|} \tanh^{|\Gamma|} \beta n(|\Gamma|) \quad (\text{A2})$$

The notation is as follows. We have a graph $G = (V, E)$ that describes our lattice, where V are the vertices and E are the edges, which are the bonds between neighboring sites. If we restrict ourselves to subgraphs with only occupied bonds allowed by the Ising model, then the degree of each vertex is even. This is the number of bonds emanating from a particular vertex. The set of edges of such a subgraph is described as being ‘‘Eulerian.’’ The space of all such sets of edges is known as the cycle space $\mathcal{C}(G)$. The notation $|V|$, $|E|$, $|\Gamma|$ denotes the number of elements in each set (cardinality). In the second line, $n(|\Gamma|)$ counts the multiplicity of subgraphs of cardinality $|\Gamma|$, and is zero when $|\Gamma|$ does not correspond to a ‘‘legal’’ subgraph.

We now specialize the presentation to the case of the two-dimensional Ising model on a square lattice with periodic boundary conditions. In this case $|V|$ is $V = L^2$, the volume that we express in lattice units, and $|E| = 2V$. We introduce the notation $t \equiv \tanh(\beta)$ and we call N_b the number of bonds in a graph (values taken by $|\Gamma|$). With these notations we recover Eq. 3.

It is this bond formulation that is the basis of both random cluster algorithms [27] and worm algorithms [18]. In this paper we utilize the latter. Both of these classes of algorithms have the benefit of significantly avoiding critical slowing down. This is essential near the critical temperature T_c .

2. Heat capacity

One striking feature of the second order transition for the two-dimensional Ising model is the logarithmic divergence of the specific heat density at the critical temperature T_c . In this section, we review the way the specific heat can be calculated with the worm algorithm and we check our answer with the exact finite volume expressions [28].

Using the standard thermodynamical formula for the

average energy

$$\langle E \rangle = -\frac{\partial}{\partial \beta} \ln Z, \quad (\text{A3})$$

with the expression Eq. (3) of Z , we get

$$\langle E \rangle = -\tanh(\beta) \left(2V + \frac{\langle N_b \rangle}{\sinh^2(\beta)} \right), \quad (\text{A4})$$

where we define

$$\langle f(N_b) \rangle \equiv \sum_{N_b} f(N_b) t^{N_b} n(N_b) / \sum_{N_b} t^{N_b} n(N_b). \quad (\text{A5})$$

We can then use

$$C_V = \frac{\partial \langle E \rangle}{\partial T}, \quad (\text{A6})$$

to write

$$\frac{C_V}{V} = \beta^2 \left[\frac{2}{\cosh^2(\beta)} - \frac{4 \cosh(2\beta)}{\sinh(2\beta)} \frac{\langle N_b \rangle}{V} \right. \quad (\text{A7})$$

$$\left. + \left(\frac{2}{\sinh(2\beta)} \right)^2 \frac{\langle (N_b - \langle N_b \rangle)^2 \rangle}{V} \right]. \quad (\text{A8})$$

Since $\frac{\langle N_b \rangle}{V} \leq 2$ (in two dimensions), the only possibly divergent part is the variance of N_b per unit volume $\langle \Delta_{N_b}^2 \rangle$ defined in Eq. (4). The singularity near T_c is known from Onsager’s solution:

$$\frac{C_V}{V} = -\frac{2}{\pi} \left(\ln(1 + \sqrt{2}) \right)^2 \ln(|T - T_c|) + \text{regular}. \quad (\text{A9})$$

This implies Eq. (5).

3. Monte Carlo implementation

We can proceed to sample the closed path configuration space using the worm algorithm [18]. A single Monte Carlo step is outlined below.

1. Randomly select a starting point on the lattice (i_0, j_0) .
2. Propose a move to a neighboring site (i', j') , selected at random.
3. If no link is present between these two sites, a bond is created with acceptance probability $P = \min\{1, \tanh \beta\}$. If the bond is accepted, we update the bond number for the present worm, $n_b = n_b + 1$.
4. If a link already exists between the two sites, it is removed with probability $P = 1$.
5. If $(i', j') = (i_0, j_0)$, i.e. we have a closed path, go to (1.). Otherwise, $(i', j') \neq (i_0, j_0)$, go to (2.)

The number of necessary Monte Carlo steps required to achieve sufficient statistics varies with the lattice size, thermalization time, and temperature. After each step, we calculate the energy in terms of the average number of active bonds N_b , and consider the system to be thermalized when fluctuations between subsequent values of the energy are less than 1×10^{-3} . We then save the resulting configuration, along with the final values for all physical quantities of interest. This process is then repeated many times over a range of different temperatures to generate sufficient statistics for physical observables. All error-bars are calculated using the block jackknife resampling technique.

4. Tests

The above formulas have been used to calculate C_V . Precise checks were performed by comparing with the exact results obtained from Ref. [28]. The agreement can be seen in Fig. 13. Results for other lattice sizes that we have simulated are similar.

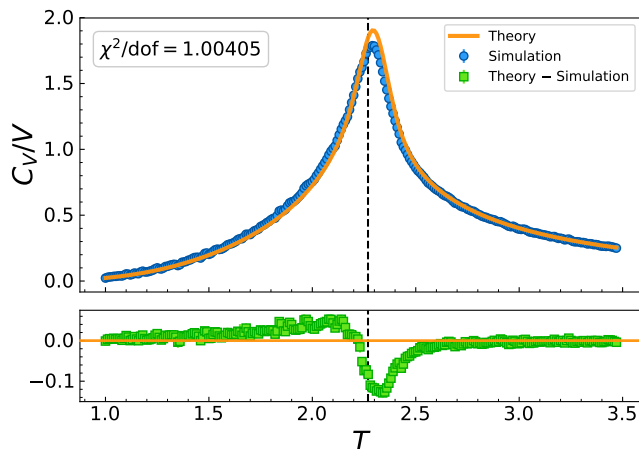


FIG. 13. Comparison of the worm Monte Carlo computation of the specific heat C_v versus temperature and the exact results using the formula in [28], for an $L = 32$ lattice. Note that χ^2/dof represents the reduced chi-squared statistic. It can be seen that the agreement is excellent, except for a slight deviation at the critical temperature, where Monte Carlo algorithms tend to face difficulties with critical slowing down. This is mostly addressed with the worm algorithm, in terms of having a dynamical scaling exponent that is zero rather than two, but there is (as can be seen), still a residual suppression of fluctuations in the immediate vicinity of T_c .

5. Conjecture about λ_{max}

Using the Monte Carlo algorithm outlined above, we can calculate the average number of occupied bonds at a particular temperature by averaging over all configura-

tions

$$\langle N_b \rangle \equiv \frac{1}{N_{\text{configs}}} \sum_{n=1}^{N_{\text{configs}}} N_b^{(n)} \quad (\text{A10})$$

$$= \left\langle \sum_{j=\text{bonds}} v_j \right\rangle \quad (\text{A11})$$

$$= 2V \langle \mathbf{v}_b \rangle. \quad (\text{A12})$$

From this, we have that

$$\langle \mathbf{v}_b \rangle = \frac{\langle N_b \rangle}{2V}, \quad (\text{A13})$$

where we have defined $\langle \mathbf{v}_b \rangle$ to be the average occupation of bonds, $N_b^{(n)}$ to be the number of occupied bonds in the n -th configuration, and we have used Eq. (6) in the second line. If we consider graphs with no self-intersections,

$$\sum_{j=\text{bonds}} v_j = \sum_{j=\text{sites}} v_j. \quad (\text{A14})$$

For small β (high T) this can be a good approximation,

$$\left\langle \sum_{j=\text{bonds}} v_j \right\rangle \simeq \left\langle \sum_{j=\text{sites}} v_j \right\rangle \implies \quad (\text{A15})$$

$$\langle \mathbf{v}_b \rangle \simeq \frac{1}{2} \langle \mathbf{v}_s \rangle \quad (\text{A16})$$

This agrees with our intuition, that the average image $\langle \mathbf{v} \rangle$ should resemble a “tablecloth”, where the site pixels are twice as dark as the link pixels. This can be seen clearly in Fig. 14.

For a general graph, a link is shared by two sites (its endpoints), whereas a site can be shared either by 0, 2, or 4 bonds. If the site is shared by two bonds, it is only visited once, denoted $\text{sites}^{(1)}$, and if it is shared by four bonds, it is visited twice, denoted $\text{sites}^{(2)}$. This allows us to break up the sum over bonds into two terms

$$\sum_{j=\text{bonds}} v_j = \frac{2}{2} \sum_{j=\text{sites}^{(1)}} v_j + \frac{4}{2} \sum_{j=\text{sites}^{(2)}} v_j \quad (\text{A17})$$

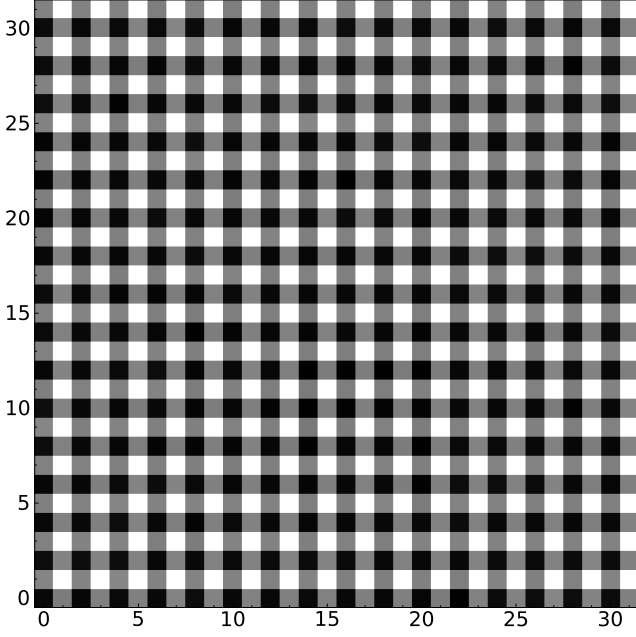


FIG. 14. Average image $\langle \mathbf{v} \rangle$ calculated for the $L = 16$ lattice at $T = 2.0$, illustrating the tablecloth-like appearance.

Rearranging and taking averages gives

$$\left\langle \sum_{j=\text{sites}^{(1)}} v_j + \sum_{j=\text{sites}^{(2)}} v_j \right\rangle \quad (\text{A18})$$

$$= \left\langle \sum_{j=\text{bonds}} v_j - \sum_{j=\text{sites}^{(2)}} v_j \right\rangle \quad (\text{A19})$$

$$= \left\langle \sum_{j=\text{sites}} v_j \right\rangle \quad (\text{A20})$$

$$= V \langle \mathbf{v}_s \rangle \quad (\text{A21})$$

$$= \left\langle \sum_{j=\text{bonds}} v_j \right\rangle - \left\langle \sum_{j=\text{sites}^{(2)}} v_j \right\rangle \quad (\text{A22})$$

$$= 2V \langle \mathbf{v}_b \rangle - \langle N_{\text{sites}^{(2)}} \rangle \implies \quad (\text{A23})$$

$$\frac{\langle N_{\text{sites}^{(2)}} \rangle}{V} = 2 \langle \mathbf{v}_b \rangle - \langle \mathbf{v}_s \rangle. \quad (\text{A24})$$

We can rewrite the last equation using (A12)

$$\langle \mathbf{v}_s \rangle = \frac{\langle N_b \rangle}{V} - \frac{\langle N_{\text{sites}^{(2)}} \rangle}{V}. \quad (\text{A25})$$

This suggests that a departure from a perfect tablecloth ($\langle \mathbf{v}_s \rangle = 2 \langle \mathbf{v}_b \rangle$) contains information. Another useful con-

struct is the covariance matrix,

$$C_{ij} = \left\langle (v_i - \langle \mathbf{v} \rangle_i) (v_j - \langle \mathbf{v} \rangle_j)^T \right\rangle \quad (\text{A26})$$

$$= \frac{1}{N_{\text{configs}}} \sum_{n=1}^{N_{\text{configs}}} \left(v_i^{(n)} - \langle \mathbf{v} \rangle_i \right) \left(v_j^{(n)} - \langle \mathbf{v} \rangle_j \right)^T, \quad (\text{A27})$$

where we have defined $v_k^{(n)}$ to be the grayscale value of the k -th pixel in the n -th sample configuration, and $\langle \mathbf{v} \rangle_k$ is the average grayscale value of the k -th pixel over the set of configurations.

At some fixed temperature, the covariance matrix, $C \in \mathbb{R}^{N_{\text{configs}} \times 4L^2}$, where N_{configs} is the number of sample configurations (images), with each configuration flattened into a vector of length $4L^2$. We can then perform a singular value decomposition (SVD) on the covariance matrix,

$$C = W \Lambda W^T \quad (\text{A28})$$

where W is a $4L^2 \times 4L^2$ matrix whose columns (\mathbf{w}_k) are the eigenvectors of C , and Λ is the diagonal matrix of the absolute value of the eigenvalues $\lambda^{(k)}$ of C , arranged in decreasing order. Without loss of generality, we can assume that the eigenvectors \mathbf{w}_k are real and normalized such that $\mathbf{w}_k^T \mathbf{w}_k = 1$. Thus, we can write

$$C \mathbf{w}_k = \lambda^{(k)} \mathbf{w}_k \quad (\text{A29})$$

$$\mathbf{w}_k^T C \mathbf{w}_k = \lambda^{(k)} \quad (\text{A30})$$

For our purposes, we are interested in the first principal component, with eigenvalue $\lambda^{(1)} \equiv \lambda_1$ and corresponding eigenvector \mathbf{w}_1 .

We conjectured that the first principal component, \mathbf{w}_1 of the covariance matrix C is directly proportional to the average worm configuration (image) $\langle \mathbf{v} \rangle$, i.e.

$$\mathbf{w}_1 \propto \langle \mathbf{v} \rangle. \quad (\text{A31})$$

From our results in II, we can write

$$\langle \mathbf{v} \rangle^2 = \langle \mathbf{v} \rangle^T \langle \mathbf{v} \rangle \quad (\text{A32})$$

$$= 2V \langle \mathbf{v}_b \rangle^2 + V \langle \mathbf{v}_s \rangle^2. \quad (\text{A33})$$

This suggests that

$$\mathbf{w}_1 = \frac{\langle \mathbf{v} \rangle}{\sqrt{(2 \langle \mathbf{v}_b \rangle^2 + \langle \mathbf{v}_s \rangle^2) V}}. \quad (\text{A34})$$

Moreover, we can write

$$\sum_i \left(v_i^{(n)} - \langle \mathbf{v} \rangle_i \right) \langle \mathbf{v} \rangle_i \quad (\text{A35})$$

$$= \left\{ \langle \mathbf{v}_b \rangle \sum_{j=\text{bonds}} v_j^{(n)} + \langle \mathbf{v}_s \rangle \sum_{j=\text{sites}} v_j^{(n)} \right. \quad (\text{A36})$$

$$\left. - \left(2V \langle \mathbf{v}_b \rangle^2 + V \langle \mathbf{v}_s \rangle^2 \right) \right\} \quad (\text{A37})$$

$$= \left\{ \langle \mathbf{v}_b \rangle N_b^{(n)} + \langle \mathbf{v}_s \rangle N_s^{(n)} \right. \quad (\text{A38})$$

$$\left. - V \left(2 \langle \mathbf{v}_b \rangle^2 + \langle \mathbf{v}_s \rangle^2 \right) \right\} \quad (\text{A39})$$

$$= \left\{ \langle \mathbf{v}_b \rangle \left(N_b^{(n)} - \langle N_b \rangle \right) \right. \quad (\text{A40})$$

$$\left. + \langle \mathbf{v}_s \rangle \left(N_s^{(n)} - \langle N_s \rangle \right) \right\} \quad (\text{A41})$$

$$\equiv \langle \mathbf{v}_b \rangle \Delta_{N_b}^{(n)} + \langle \mathbf{v}_s \rangle \Delta_{N_s}^{(n)}. \quad (\text{A42})$$

From this, we can extract a relationship between the eigenvalue corresponding to the first principal compo-

nent, $\lambda^{(1)}$ and the fluctuations Δ_{N_b} and Δ_{N_s} ,

$$\begin{aligned} \mathbf{w}_1^T C \mathbf{w}_1 &= \lambda^{(1)} \\ &= \frac{1}{N_{\text{configs}}} \sum_{n=1}^{N_{\text{configs}}} \left(\langle \mathbf{v}_b \rangle^2 \left(\Delta_{N_b}^{(n)} \right)^2 \right. \\ &\quad \left. + 2 \langle \mathbf{v}_b \rangle \langle \mathbf{v}_s \rangle \Delta_{N_b}^{(n)} \Delta_{N_s}^{(n)} + \langle \mathbf{v}_s \rangle^2 \left(\Delta_{N_s}^{(n)} \right)^2 \right) \\ &\quad \frac{1}{\left(2 \langle \mathbf{v}_b \rangle^2 + \langle \mathbf{v}_s \rangle^2 \right)} \end{aligned}$$

Now, if we consider the high temperature approximation where sites only have single visits (no self-intersections), $\langle \mathbf{v}_s \rangle \simeq 2 \langle \mathbf{v}_b \rangle$, $\langle N_s \rangle \simeq \langle N_b \rangle$, and $\Delta_{N_b} \simeq \Delta_{N_s}$, we have that $2 \langle \mathbf{v}_b \rangle^2 + \langle \mathbf{v}_s \rangle^2 \simeq 6 \langle \mathbf{v}_b \rangle^2$ and

$$\lambda_1 \simeq \frac{\langle \mathbf{v}_b \rangle^2}{N_{\text{configs}}} \frac{9}{6 \langle \mathbf{v}_b \rangle^2} \sum_{n=1}^{N_{\text{configs}}} \left(\Delta_{N_b}^{(n)} \right)^2 \quad (\text{A43})$$

$$= \frac{3}{2} \frac{1}{N_{\text{configs}}} \sum_{n=1}^{N_{\text{configs}}} \left(\Delta_{N_b}^{(n)} \right)^2 \quad (\text{A44})$$

$$= \frac{3}{2} \langle \Delta_{N_b}^2 \rangle. \quad (\text{A45})$$

A justification for making this approximation can be seen in Fig. 15.

6. Illustration of alternate blockings

Appendix B: Possible applications: From Images to Loops

Having better understood how these RG transformations can be used to describe the 2D Ising model near criticality, we began to look for possible applications to real-world datasets. For our analysis, we used the CIFAR-10 [29] image set consisting of 60,000 32×32 color images in 10 classes. First, each of the images were converted to a grayscale with pixel values in the range $[0, 1]$. Next, a grayscale cutoff value was chosen so that all pixels with values below the cutoff would become black, and pixels above the cutoff would become white, resulting in images consisting entirely of black and white pixels. Finally, each of these images were converted to ‘worm-like’ images by drawing the boundaries separating black and white collections of pixels. An example of these prepro-

cessing steps are illustrated in Fig. 17. This process was carried out on a mini-batch consisting of 500 randomly selected images from the CIFAR-10 image set. For each image in our mini-batch, we calculated $\langle N_b \rangle$ and $\langle \Delta_{N_b}^2 \rangle$ over a range of grayscale cutoff values in $[0, 1]$ in steps of 0.02. Each of these images were then iteratively blocked using the $(1 + 1 \rightarrow 0)$ blocking procedure described in Sec. IV, calculating $\langle N_b \rangle$ and $\langle \Delta_{N_b}^2 \rangle$ for each successive blocking step, as shown in Fig. 18. Immediately we see that there is no identifiable low temperature phase, and that for cutoff values near both 0 and 1, we obtain images which are mostly empty, similar to the high temperature configurations obtained from the worm algorithm. This suggests that there is no such notion of criticality (as characterized by the abrupt transition from a low to high temperature phase) like we found for the two-dimensional Ising model.

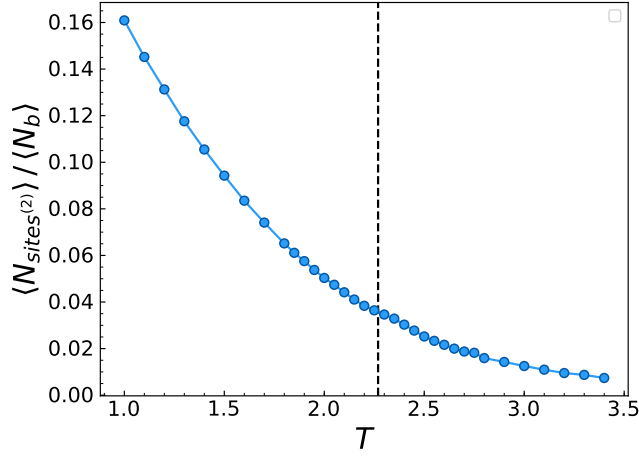


FIG. 15. Ratio of the number of twice visited sites $\langle N_{sites^{(2)}} \rangle$ to the average number of bonds $\langle N_b \rangle$ versus temperature, for the $L = 32$ lattice. This clearly justifies our approximation $\langle \mathbf{v}_s \rangle \simeq 2\langle \mathbf{v}_b \rangle$, where we ignore the contribution from twice visited sites.

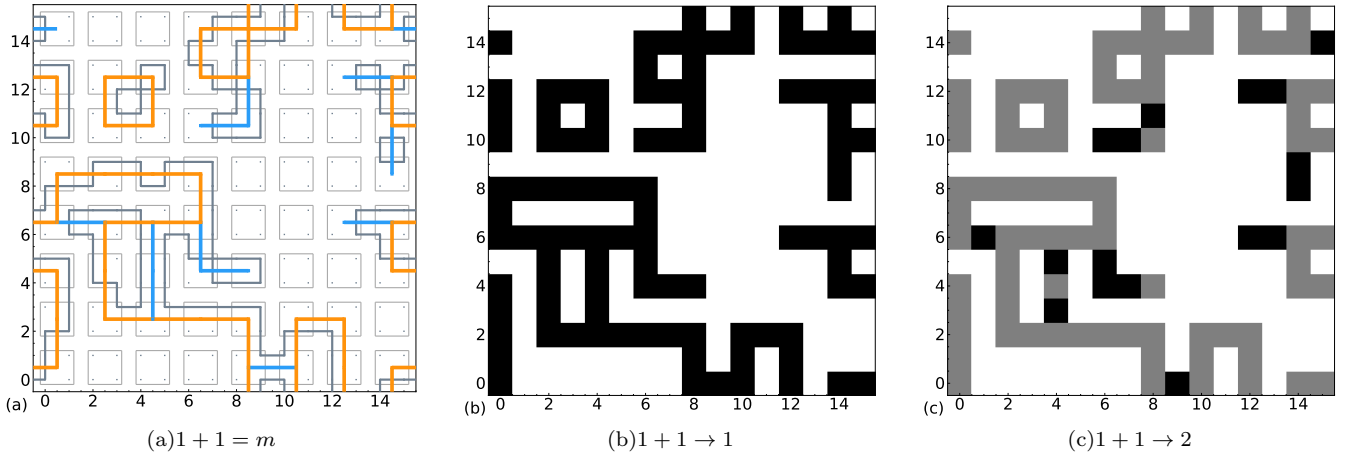


FIG. 16. Example of the different coarse-graining (“blocking”) procedures applied to a sample worm configuration generated at $T = 2.0$. Note that in (16(a)) $m \in \{1, 2\}$, and double bonds are represented by blue lines. (16(b)), (16(c)), illustrate the results of applying different weights to the so-called “double bonds” in the images representing a blocked configuration. Note that in (16(b)) $1 + 1 \rightarrow 1$, double bonds are given the same weight as single bonds, and in (16(c)) $1 + 1 \rightarrow 2$, double bonds are given twice the weight as single bonds, appearing twice as dark.

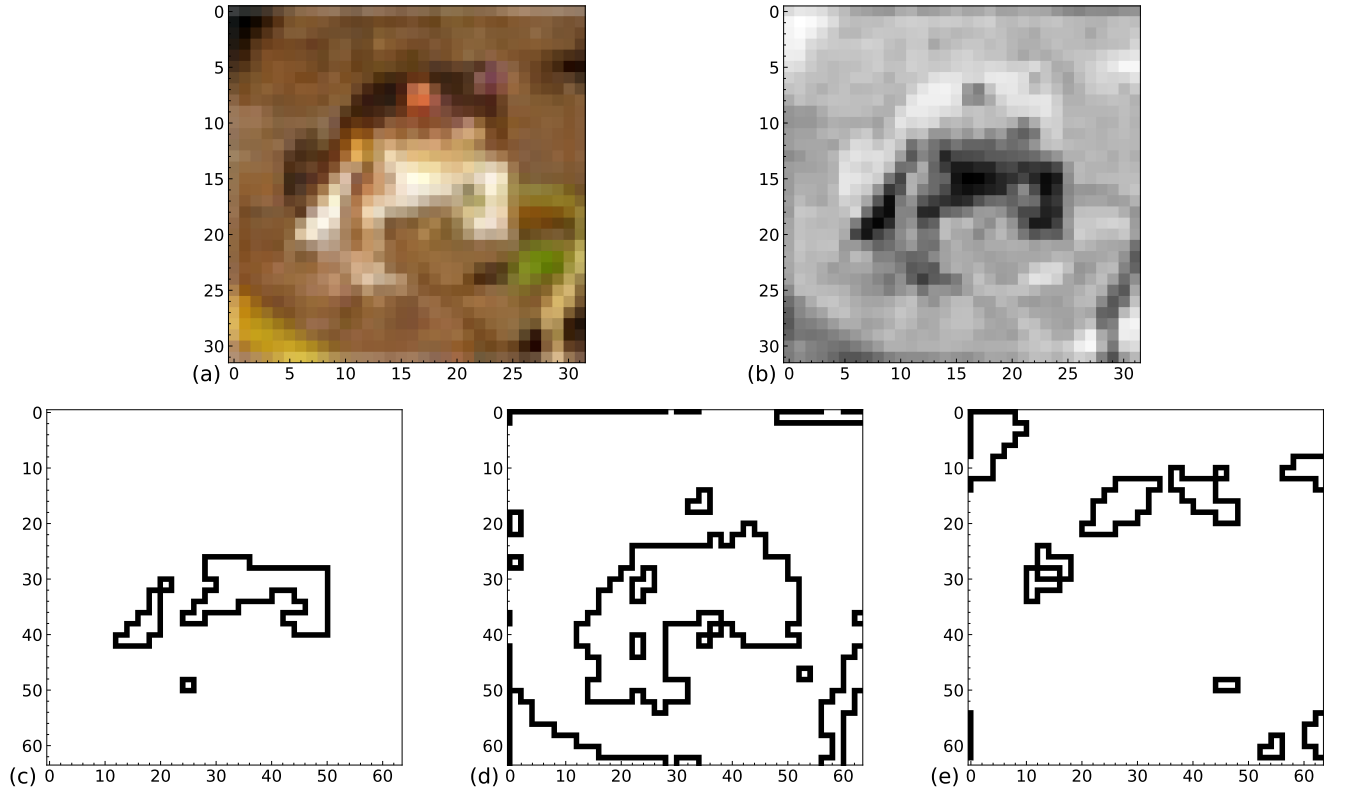


FIG. 17. Example of preprocessing steps for converting CIFAR-10 images to ‘worm-like’ images, illustrating the resulting image for different values of the grayscale cutoff. (a) Original image from CIFAR-10 dataset. (b) Image converted to grayscale. (c) Resulting image from cutoff values of 0.25, (d) 0.5, and (e) 0.75.

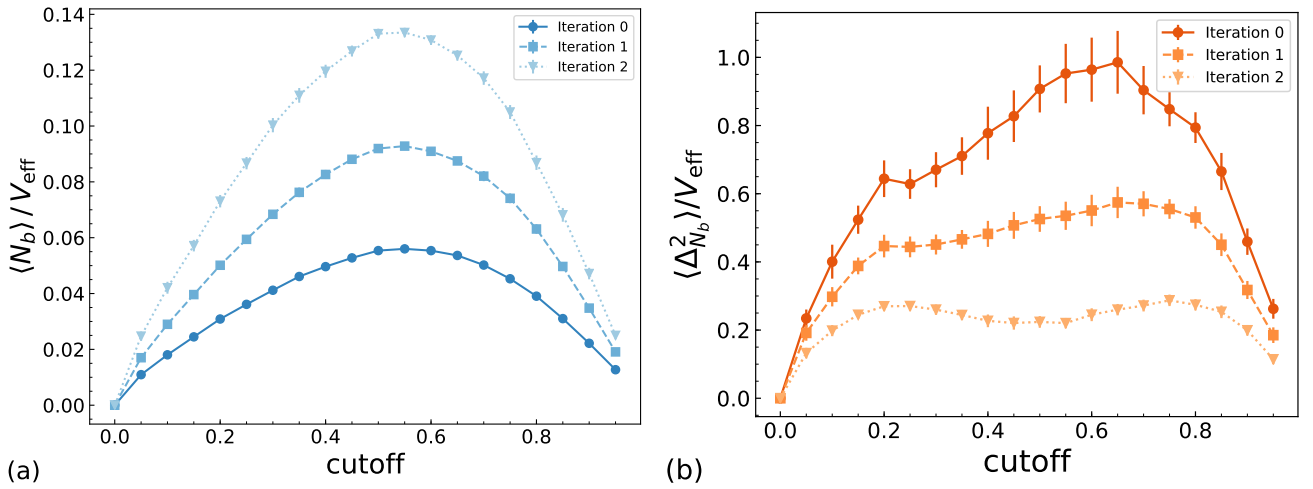


FIG. 18. $\langle N_b \rangle$ and $\langle \Delta_{N_b}^2 \rangle$ vs. grayscale cutoff value for 500 randomly chosen images from the CIFAR-10 dataset.